

# Measurement of Colliding Beam Parameters with Wide Angle Beamstrahlung

G. Bonvicini, D. Cinabro and E. Luckwald  
*Wayne State University, Detroit MI 48201*

May 2, 2019

## 1 Introduction

Machine issues at particle factories are dominated by luminosity optimization, which is the overlap of the density functions  $\rho$  of the two beams over space and time. For a single beam crossing,

$$L = c \int dV d\tau \rho_1(\mathbf{r}, \tau) \rho_2(\mathbf{r}, \tau), \quad (1)$$

where  $dV$  is the volume element and  $\tau$  is a time variable of order of the beam-crossing duration. Optimal luminosity is achieved by perfect transverse overlap of two equal and Gaussian beams squeezed to the limit allowed by the tune shift. For a single beam crossing, that reads

$$\begin{aligned} L_0(t) &= \frac{N_1(t)N_2(t)c}{(2\pi)^3\sigma_x(t)\sigma_y(t)\sigma_z(t)} \int dV d\tau e^{-(x^2/\sigma_x^2(t)+y^2/\sigma_y^2(t)+(z^2+(c\tau)^2)/\sigma_z^2(t))} \\ &= \frac{N_1(t)N_2(t)}{4\pi\sigma_x(t)\sigma_y(t)}, \end{aligned} \quad (2)$$

where the  $N_{1,2}$  and  $\sigma_{x,y,z}$  are the beam populations and spatial dimensions at any given time  $t$  (which is a run-time variable of order one hour).

This formula becomes rather complex over time. Particles are deflected by the other beam at each crossing, significantly affecting the Twiss matrix of the machine. The beam currents  $N_i(t)$  decrease due to beam lifetime also causing the machine's Twiss matrix to drift. If the machine is perfectly symmetric, the transverse dimensions will change but the beams will maintain perfect overlap.

Even symmetric machines have some degree of asymmetry, and beams start moving independently in the transverse plane as soon as the run starts. At *B*-Factories such as CESR, PEP-II, and KEK, beams have horizontal dimensions  $\sigma_y$  of order several microns, with aspect ratios  $\epsilon = \sigma_y/\sigma_x \sim 0.02 - 0.04$ . A drift of 5 microns is enough to spoil the luminosity.

A better description of the luminosity over time should be

$$L(t) = L_0(t)(1 - w(t)). \quad (3)$$

$w(t)$  is the positive-defined waste parameter due to non-instantaneous optimal overlap. If  $w(t)$  is known, the wasted integrated luminosity is defined as

$$L_w = f \int dt L_0(t)w(t), \quad (4)$$

where  $f$  is the machine frequency. The waste parameter can be readily derived from the convolution integrals, Equations 1 and 2. Dropping the time dependence, one gets

$$w = 1 - \frac{L}{L_0}. \quad (5)$$

The waste parameter is clearly of great interest, and one of the most important issues not only at *B* factories but also at future linear colliders. As soon as  $w$  is non-zero, a correction should be applied to restore optimal luminosity. The ability to measure and reduce  $w$  would make for a substantial increase in the delivered luminosity of any machine.

Although  $w$  can be defined mathematically from Equation 3, the beam-beam topology cannot be measured directly. Techniques have been developed that measure the transverse displacement of the centers of gravity of the beams by Bambade[1] and Sagan, Sikora and Henderson[2]. Both of these techniques actively displace one of the beams, and monitor the other beam to observe the strength of the beam-beam interaction. In practice these techniques are sensitive to the relative displacement of the beams centers from optimal beam-beam overlap.

Generally, a discussion of the waste parameter must include all possible degrees of freedom in the evolution of a machine over a run. There are seven parameters which can affect optimal beam-beam overlap[3]. These are shown in Figure 1. Briefly there is a transverse displacement between the two beam centers described by a vector  $(\Delta x, \Delta y)$ , the transverse sizes of the two beams  $\sigma_{x1}$ ,  $\sigma_{y1}$ ,  $\sigma_{x2}$ , and  $\sigma_{y2}$ , and a relative rotation of the two beams  $\phi$ . The two beam currents also affect the beam-beam interaction. Currents are easily monitored and are not included in the discussion below.

In this paper, a technique is proposed by which six of the seven parameters can be passively monitored with the observation of wide angle beamstrahlung. In case of non-zero waste, which is called a “pathology”, the responsible parameter is identified unambiguously, and the amount of needed correction is measured. The seventh parameter can easily be measured in a beam scan also using the wide angle beamstrahlung signal.

Seven parameters to characterize the beam-beam collision is a large number. It is easiest to discuss the problem if it is broken into two parts.

- The machine is perfectly symmetric, that is, the machine optics is exactly the same for both beams. In Figure 1, that means that the two beams have zero offsets, zero rotation, and the same transverse dimensions, resulting in only two parameters. Dropping indices, they are the transverse dimensions  $\sigma_x$  and  $\sigma_y$ . If the machine is symmetric, beams maintain optimal overlap, but the optics is affected by the varying currents. The luminosity is determined by the transverse size of the beam. The case of measuring the transverse beam size is discussed in Section 3.
- The beams move independently in the transverse plane due to machine asymmetry decreasing overlap and luminosity. In section 4 the measurements of the relative sizes of the two beams, their transverse displacement, and the angle between them are described.

In this paper the use of large angle beamstrahlung, which is described in detail in reference[3], is described as a beam-beam monitor that allows complete control over both the beam-beam interaction strength and transverse displacements. Large-angle beamstrahlung observables, combined in a simple 2-dimensional diagram which is called the beamstrahlung diagram, monitors the wasted luminosity.

In Section 2 the information content of large angle beamstrahlung is discussed. Section 3 covers the symmetric machine case, concentrating on measurements of the beam size. Section 4 covers asymmetric machines, introduces the beamstrahlung diagram, and shows how the waste parameter can be measured. The use of the beamstrahlung diagram to eliminate wasted luminosity is shown in Section 5. Three appendices are included for completeness. Appendix A derives in a simple way three crucial properties of large angle synchrotron radiation. Appendix B provides a description of the beam-beam simulation developed for this paper and Appendix C evaluates the simulation’s accuracy.

## 2 Large Angle Beamstrahlung

The properties of large angle radiation, emitted by a ultra-relativistic particle, differ dramatically from the classical synchrotron radiation formulae[4]. Appendix A shows that the approximations used in reference [3] and in this paper are valid at large angles for all present and proposed  $e^+e^-$  colliders, if beamstrahlung detection is to be done at or near the “magic angle” described in [3]. Three properties of large angle radiation are derived in Appendix A. Of particular interest is the 100% linear polarization, either parallel or perpendicular to the bending force, obtained at certain azimuthal locations at large angle.

At CESR for example, it is possible to detect such radiation in visible light at a location 5 meters away from the interaction point, at a 6mrad angle. The beam-beam interaction occurs over a volume of order  $300\mu\text{m}\times 7\mu\text{m}\times 7\text{mm}$ , and particles are typically deflected laterally by  $10^{-2}$  mrad. Thus the light detector is seen at the same angle by all of the beam, and throughout the dynamic beam-beam collision. These are the conditions termed as “CESR conditions” and used for the calculations of Sections 4 and 5. A fixed fraction of the beamstrahlung energy is collected at such a location, effectively measuring the total energy up to a constant. Different polarization components can also be easily observed, by filtering the observed light through polarimeters.

The two polarization components can be used to build the radiation vectors  $\mathbf{U}_1$  from one beam and  $\mathbf{U}_2$  from the other beam, which are two-dimensional vectors in the first quadrant. The first dimension is the horizontal component of the polarized beamstrahlung power signal and the second is the vertical. The total energy vector  $\mathbf{U}$  is defined as  $\mathbf{U}_1 + \mathbf{U}_2$ . At large angles the polarization components and radiation spectrum factorize[6] and a different orientation of the polarimeters would simply rotate the horizontal and vertical axes..

As mentioned in the Introduction, at present and proposed machines, beams are very flat ( $\epsilon \sim 0.02 - 0.04$ ). It is convenient to develop the theory only for flat beams which leads to two simplifications. First, terms of order  $\epsilon$  and higher can be neglected in equations as needed. Second, a natural preferred orientation exists in the transverse plane, which is adopted to produce the results of this paper.

It should be noted that two counters on each side, each looking at a different polarization component, and in absence of background, are enough to extract complete information from beamstrahlung. As an example, given the

formulae in Appendix A,  $U_x$  can be measured by measuring the  $x$ -polarized component at zero degrees in azimuth, and  $U_y$  by the  $x$ -polarized component at 45 degrees.

### 3 Symmetric Machines

If a machine is perfectly symmetric, the beam currents and transverse dimensions of the beams will evolve, while maintaining perfect overlap. Measurements of the beam sizes  $\sigma_x$  and  $\sigma_y$ , determine the luminosity. In this case most of the interplay between machine and beam-beam interaction is through the dynamic beta effect.

The dynamic beta effect is proportional to the average electric field seen by one particle over many beam crossings, hence it is proportional to the charge in the other beam, times the average inverse impact parameter  $b$  between particles of beam 1 and particles of beam 2[7],

$$\langle \mathbf{E}_1 \rangle \propto N_2 \langle \frac{\mathbf{b}}{b^2} \rangle . \quad (6)$$

From[6] the beamstrahlung energy is proportional to

$$U_1 \propto N_1 \langle E_1^2 \rangle , \quad (7)$$

or

$$\langle E_1^2 \rangle \propto U_1/N_1 . \quad (8)$$

The  $\langle E_1 \rangle$  and  $\langle E_1^2 \rangle$  are related through the transverse shape of the beam, which can be taken to be Gaussian with no loss of precision. Therefore, monitoring the dynamic beta effect can be done efficiently by monitoring the  $U_i$  and the  $N_i$  at the same time.

Equation 7 can be rewritten as[3, 6]

$$U_1 \propto \frac{N_1 N_2^2}{\sigma_x^2 \sigma_z} f(\epsilon) . \quad (9)$$

The beam length,  $\sigma_z$ , is usually constant, and will not be considered here, but clearly a beamstrahlung detector can also be used to monitor the beam length, for example during machine studies. The function  $f(\epsilon)$  varies slowly

$$f(\epsilon) \sim 1 + 11.4\epsilon, \quad (10)$$

and can be considered nearly constant in the following.

The result above assumes “stiff” beams. A stiff beam is one where the beam particles do not change their transverse position appreciably during the collision. Appendix B shows that dynamic effects are negligible.

In flat beams most of the impact parameter is due to the distance in  $x$  between the particles, and the energy radiated is almost only dependent on  $\sigma_x$ . For perfect overlap of stiff Gaussian beams the energy  $U$  is unpolarized[6]. No information can be extracted out of polarization, and beamstrahlung cannot monitor passively symmetric changes in  $\sigma_y$ . The total power radiated is thus sensitive to  $\sigma_x$ .

However, as pointed out in references[3, 6], a scan of one beam along the vertical axis will produce the characteristic camelback feature in the plot of  $U$  versus the beam-beam offset seen in Figure 3, which has already been used in the detection of beamstrahlung[8]. The  $\sigma_y$  can be precisely determined by measuring the peak-valley distance  $d$  shown in Figure 3. The relation between  $d$  and  $\sigma_y$  is

$$d \sim 3.97\sigma_y(1 - 5.4\epsilon). \quad (11)$$

Currently, the CESR beams are artificially perturbed with an amplitude of order  $0.01\sigma_y$  to measure the beam-beam interaction by observing the effect of the perturbation on the other beam via the lock-in effect[2]. It is conceivable that this technique could ultimately be used to determine  $\sigma_y$  without scanning. Note that a beam scan could also be used to measure  $\sigma_x$  separating it from  $\sigma_z$ .

A beamstrahlung monitor can be very useful even when a machine is perfectly symmetric, allowing purely passive monitoring of the beam-beam interaction and thus the beam length or  $\sigma_x$ . It can be used to measure  $\sigma_y$  in a beam scan. The next Section, which deals with purely asymmetric pathologies, shows that this method is truly valuable when beams are not colliding head on in the transverse plane and may have different transverse sizes.

## 4 Asymmetric Machines

If a machine is asymmetric, as all real machines are to some degree, the two beams will drift independently in the 7-dimensional space that induces luminosity waste. For the purpose of studying asymmetric machines, a single pass beam-beam simulation program was written. The program generates complex beam-beam configurations involving all the pathologies shown in Figure 1. These configurations are, in principle, computable analytically in

Parameter	Symbol	Value
Beam Width	$\sigma_x$	300 $\mu\text{m}$
Beam Height	$\sigma_y$	7 $\mu\text{m}$
Beam Length	$\sigma_z$	1.8 cm
Bunch Charge	$N$	$11 \times 10^{10}$
Relativistic Factor	$\gamma$	$10^4$

Table 1: Beam parameters chosen for the simulation results presented here.

the limit of stiff beams. It was important also to cross-check the effects of beam-beam dynamics, as the particles of one beam are deflected towards the center of the other beam. The latter is an effect that must be computed by simulation.

The simulation program is described in Appendix B. Its precision is evaluated in Appendix C and is found to be between 0.1% and 0.2%, for beamstrahlung yields, and better than 1%, for the luminosity enhancement due to beam-beam pinching. The nominal conditions to produce results in this paper were chosen as in Table 4 and are appropriate for *B*-Factories. The measurement of the two beam sizes was discussed in the previous section. The remaining five parameters are discussed here: two relative transverse dimensions; two offsets; and one angle. Present day beam position monitors have spatial resolutions of order 20  $\mu\text{m}$ , which is substantially less than the  $\sigma_x$  of these beams, and should always provide adequate overlap along the  $x$ -axis leaving four pathologies of concern. An offset in  $x$  will generate a unique configuration of the beamstrahlung diagram, which mirrors the one obtained for an offset in  $y$  which is discussed below, and can be analyzed in a completely equivalent way.

For simplicity it is assumed that only one beam is developing a pathology at any given time. The four pathologies that lead to wasted luminosity are shown in Figure 4. They correspond respectively to a vertical offset, imperfect vertical focusing, imperfect horizontal focusing, and a rotation of one beam with respect to the other. All these pathologies except the third have been observed at CESR.

The expected value of each polarization component is also assumed, for optimal beam-beam collision, which we call  $U_0$ . In practice  $U_0$  can be measured experimentally by continuous observation of colliding beams, or by separately determining the beam currents, and  $\sigma_x$  and  $\sigma_y$  with a beam-beam

scan as discussed in the previous section.

The beamstrahlung diagram plots  $\mathbf{U}_1, \mathbf{U}_2$  normalized by  $U_0$ . In the figures below the contribution from the pathological beam is represented by the dashed arrow. The diagram has four degrees of freedom. The total power monitors the beam-beam interaction strength, and three independent dimensionless asymmetries can be defined.

As mentioned in Section 3 if the collision is perfect and the beams are stiff the beamstrahlung radiation is unpolarized. Thus the normalized  $U_i$ 's are equal and the vector from each beam in a perfect head-on collision are on top each other at 45 degrees as shown in Figure 4. With the  $U_0$  normalization one obtains the perfect collision point at (1,1) for both beams.

The effect of dynamic beams can be estimated from Table 2 in Appendix C. For example at CESR dynamic beams increase  $U_x$  by 0.9% and  $U_y$  by 2.7%, moving the perfect collision axis 0.5 degrees above 45 degrees. Such a small modification is nearly invisible in Figure 4 and can be neglected.

Figure 5 shows for stiff beams the beamstrahlung diagrams for each pathology shown in Figure 3. Each has a unique pattern, which a feedback algorithm can discern and correct. In general, if beam 1 is smaller in  $x(y)$  than beam 2, then it will radiate less energy in  $x(y)$ .

Figure 6 is the same as Figure 5, but for dynamic beams. Comparison of the two figures shows very little difference. The effect of dynamic beams is small. Thus the beamstrahlung diagram presented in this paper is a universal display of the pattern associated with beam-beam pathologies at CESR, PEP-II, KEK, and in the future at a  $\sim 1$  TeV  $e^+e^-$  machine.

Figure 7 is the same as Figures 5 and 6, but with an offset in  $x$ ,  $18\mu\text{m}$ , or  $0.06\sigma_x$ , comparable to the resolution of beam position monitors. Again very little change is observed with respect to Figure 5 showing that small horizontal offsets have small impact.

Asymmetries corresponding to each pathology in Fig. 3 are defined as

$$A_1 = (U_y/U_x - 1)\Theta(U_y/U_x - 1), \quad (12)$$

$$A_2 = (U_{2y}/U_{1y} - 1)\Theta(U_{2y}/U_{1y} - 1), \quad (13)$$

$$A'_2 = (U_{2x}/U_{1x} - 1)\Theta(U_{2x}/U_{1x} - 1), \quad (14)$$

$$A_3 = |\sin(\mathbf{U}_1, \mathbf{U}_2)|, \quad (15)$$

where  $\Theta$  is the Heaviside function meaning in this case that the asymmetries  $A_i$  are not defined when the argument of the Heaviside function becomes negative. The indexing was chosen to indicate that the second, a beam bloated vertically, and third, a beam bloated horizontally, pathologies are generated



from both a zero dipole moment and a non-zero quadrupole moment in the transverse charge distribution, and as such they should be equally ranked.

These asymmetries are not independent. The usefulness of these beamstrahlung asymmetries is shown in Figure 8 which displays their dependence on the waste parameter defined in Equation 3. Each asymmetry's contribution to the waste parameter of Section 1 is

$$w_i \sim \frac{\partial w}{\partial A_i} A_i. \quad (16)$$

but they can not be summed together because they are not independent.

Evidence is provided in the next Section that the asymmetries should be minimized strictly in the order defined by Eqs. 12-15. In short, the total waste parameter can be defined as

$$w \sim \sum_i \hat{\partial} w_i A_i, \quad (17)$$

where the hatted derivative is defined as

$$\hat{\partial} w_i = \left( \frac{\partial w}{\partial A_i} \right)_{A_j = \min., j < i}. \quad (18)$$

Eq. 17 represents the main result of this paper. The derivatives are computed, the asymmetries are measured, and the waste parameter is obtained. Note that if the asymmetries were completely independent, the specifications  $A_j = \min.$  would have been unneeded. Asymmetries 2 and 2' represent both quadrupole corrections, and can be interchanged without harm.

For horizontal offsets between the two beams an asymmetry

$$A'_1 = (U_x/U_y - 1)\Theta(U_x/U_y - 1) \quad (19)$$

can be defined.

We note that for a 10% change in luminosity, the values of the asymmetries change by 0.1 for  $A_1$  and  $A'_1$ , 0.25 for  $A_2$  and  $A'_2$  and 0.05 for  $A_3$ . Thus these asymmetries have excellent sensitivity to wasted luminosity.

## 5 The Virtual Operator

Here examples are shown of how the beamstrahlung diagram and the asymmetries defined in Equations 12-15 and 19 can be used to eliminate wasted

luminosity even in the presence of multiple pathologies in the beam-beam collision.

We demonstrate this by studying the complete set of six double pathologies, shown in Figure 9, which can be derived from the four single pathologies shown in Figure 3. Figure 10 represents the beamstrahlung diagrams corresponding to the pathologies displayed in Figure 9. A feedback program, dubbed the Virtual Operator, finds the highest-ranking asymmetry, minimizes it by changing the appropriate collision parameter, and obtains the beamstrahlung diagrams of Figure 11, displaying only one pathology which is trivial to correct.

Two comments are in order. First, if the largest asymmetry were to be corrected first, instead of the highest-ranked, convergence would not be achieved. To prove the point, it is enough to compare Figs. 5b, 10d and 11d. If the sextupole correction is acted upon first,  $A_3$  would have to increase as opposed to being minimized.

Second, we wish to prove that minimization of a higher-ranked asymmetry effectively corrects the associated pathology. Although all the double pathologies were tried, only Fig. 9c, which corresponds to a vertical offset plus a rotation, is presented.  $A_1$  and  $A_3$  are the two most correlated asymmetries. The asymmetry  $A_1$  is not zeroed, and cannot be zeroed by moving one beam. Figure 12 shows the dependence of  $A_1$  versus the vertical offset, showing that minimization of the asymmetry gives the desired correction.

We did not consider horizontal offsets here, but they could easily have been included, as discussed in the previous Section.

## 6 Conclusion

The beamstrahlung diagram and asymmetries derived here demonstrate a complete and rigorous method for luminosity optimization. The wasted luminosity is for the first time related to quantities that are instantaneously observable, and specify the necessary correction. We have considered a complete class of beam-beam pathologies.

If the machine is perfectly symmetric a beamstrahlung monitor is very useful for measuring the size of the beam. In the case of asymmetric beams a beamstrahlung monitor is extremely powerful. The study of the beamstrahlung diagram derived from the power and polarization of the beamstrahlung signal allows identification of the beam-beam pathology, identification of the “bad” beam, and measures the correction that needs to be ap-

plied. In short the wide angle beamstrahlung signal analyzed in the manner described here is a powerful tool to eliminate wasted luminosity at present and future  $e^+e^-$  colliders.

## Appendix A

The properties of short magnet radiation were first discussed by Coisson in reference [9]. In the classical model[4], the bent electron is made to sweep through the detector in a “searchlight” fashion, effectively covering all beam-detector angles. In the Coisson’s model the opposite extreme is adopted, and the angle is kept constant throughout the orbit, the large angle approximation. Both models predict the same power, the same total polarization, and the same typical angle, of order  $1/\gamma$  for the emitted radiation, but they differ dramatically in the spectrum at large angles.

The Coisson model is of interest here because the detector’s angle is constant throughout the collision at colliders such as CESR. At large angle the classical model predicts a steep fall-off of the power, exponential both in the photon energy and in the cube of the observation angle. The Coisson model predicts three properties of large angle beamstrahlung radiation. They are:

- The cutoff energy, at large angle, does not depend on  $\gamma$ . There is no exponential fall-off as predicted by the “searchlight” approximation, making detection possible. In particular at 6 mrad at CESR, for example, visible radiation is at or below the cutoff frequency.
- The polarization is linear at a fixed location in azimuth with an eight-fold pattern,  $(\cos^2 2\phi, \sin^2 2\phi)$  around the azimuth. The angle  $\phi$  is the angle between the net transverse force experienced by the beam and the detector location. Thus the pattern of the polarization provides information about the beam-beam overlap.
- The large angle double differential spectrum is proportional to  $(\gamma\theta)^{-4}$ , and not exponential. The large angle power scales as  $1/\gamma^2$ . Thus the situation at  $B$  factories is more favorable than at higher energy machines.

These properties are re-derived here in an elementary way for constant large angle of detection. Consider an extremely relativistic particle,  $\gamma \gg 1$ , undergoing a vertical deflection, due for example to a horizontal dipole magnet exerting a force  $F$  over a length  $\sigma_z$ . Radiation of energy  $k = h\omega$

is detected at an angle  $\theta$  which is much larger than  $1/\gamma$ . In the laboratory frame the radiated energy is equal to [4]

$$U = \frac{2}{3} \frac{r_e}{mc^2} \gamma^2 F^2 \sigma_z. \quad (20)$$

A simpler derivation is possible by studying the radiation in the rest frame of the radiating particle. Note that all quantities in the particle rest frame are starred as shown in Figure 13. The radiation will have a dipole pattern with angular intensity proportional to the squared sine of the angle between the direction of detection and the direction of the force. The force maintains its vertical direction and has a modulus

$$F^* = 2\gamma F. \quad (21)$$

The angle is very large in the laboratory frame, and the corresponding direction in the rest frame is very close to the backward direction. In a perturbative treatment the angle  $\theta^*$  is taken with respect to the direction opposite the direction of motion (Fig. 13). If only small angular components along the direction of the force are considered

$$I(\theta^*) \propto \cos^2 \theta^*. \quad (22)$$

The intensity is essentially constant at small angles in the rest frame.

The relation between the energies and angles in the lab and radiating particle rest frames is given by

$$k = \frac{k^* \gamma \theta^{*2}}{2}, \quad (23)$$

$$\omega = \frac{\omega^* \gamma \theta^{*2}}{2}, \quad (24)$$

$$\theta = \frac{2}{\gamma \theta^*}. \quad (25)$$

The direction of the radiation in the radiating particle rest frame is at CESR, for example,  $\theta^* \sim 0.03$  or two degrees away from the backward axis.

In the radiating particle rest frame the cutoff frequency is inversely proportional to the duration of the perturbation, which is  $\sigma_z^*/c$ . Using equations 24 and 25, and the relativistic formula length-dilation, the following relations are obtained

$$\sigma_z^* = \sigma_z / \gamma, \quad (26)$$

$$\omega_c^* \sim O\left(\frac{c}{\sigma_z^*}\right) \quad (27)$$

$$\omega_c \sim O\left(\frac{c}{\sigma_z \theta^2}\right), \quad (28)$$

which shows that the cutoff frequency at large angle does not depend on  $\gamma$ , the first prediction by the Coisson model. At CESR,  $\omega_c \sim 10^{16} \text{sec}^{-1}$ , which is of order of the visible light frequency.

The polarization vector of the emitted radiation in the radiating particle rest frame is given by [4]

$$\mathbf{E}^*(R) = \frac{e}{mRc^2} \mathbf{n}^* \times (\mathbf{n}^* \times \mathbf{F}^*), \quad (29)$$

where  $\mathbf{n}^*$  is the unit vector along the direction of observation.

Using Equation 29, and the condition of orthogonality between  $\mathbf{E}^*$ ,  $\mathbf{B}^*$  and  $\mathbf{n}^*$ , the three vectors are

$$\mathbf{E}^* = K(\theta^{*2} \sin \phi \cos \phi, \theta^{*2} \sin^2 \phi - 1, -\theta^* \sin \phi) \quad (30)$$

$$\mathbf{B}^* = K(-1 + \theta^{*2}/2, 0, -\theta^* \cos \phi), \quad (31)$$

$$\mathbf{n}^* = (\theta^* \cos \phi, \theta^* \sin \phi, -1 + \theta^{*2}/2), \quad (32)$$

with  $K$  a constant. The polarization component along  $x$  and  $y$  in the laboratory frame are

$$E_x = \gamma(E_x^* - B_y^*) = +K \frac{\gamma \theta^{*2}}{2} \sin 2\phi = +K \frac{2}{\gamma \theta^2} \sin 2\phi \quad (33)$$

$$E_y = \gamma(E_y^* + B_x^*) = -K \frac{\gamma \theta^{*2}}{2} \cos 2\phi = -K \frac{2}{\gamma \theta^2} \cos 2\phi. \quad (34)$$

Thus each component has four azimuthal zeros, and information is replicated every 45 degrees, which is the second prediction of the Coisson model.

The total energy radiated in the laboratory frame can be expressed as an average over the boosted photon energies in the rest frame, times the number of photons  $N$

$$U = \sum \gamma(k^* + k_z^*) = N \langle \gamma(k^* + k_z^*) \rangle = N \gamma \langle k^* \rangle. \quad (35)$$

The energy flowing into a detector covering a solid angle  $d\Omega$ , located at large angle, can be easily computed in the radiating particle frame. Using  $I(\theta^*) \sim 1$ , Equations 23 and 25, and neglecting factors of order one an expression for the large angle spectrum is obtained,

$$\Delta U \sim N \theta^* \Delta \theta^* \Delta \phi \frac{\gamma \langle k^* \rangle \theta^{*2}}{2} = \frac{8U}{\gamma^4 \theta^5} \Delta \theta \Delta \phi. \quad (36)$$

The energy in the lab frame,  $U$ , contains a dependence on  $\gamma^2$ . The angular factor integrates to a constant (which agrees with Equation 8 in Ref. [3]), leaving the  $1/\gamma^2$  dependence. This is purely due to kinematics. At CESR, for example, 10nW of visible beamstrahlung are available between 6 and 7 mrad.

## Appendix B

A beam-beam interaction simulation was developed from the program described in reference [10]. Gaussian beams in all three dimensions are assumed. Beams are sliced in 3-dimensional cells. The cells are typically  $0.25-0.5\sigma$  along each axis and extend out to  $3-4\sigma$  in each direction. Thus a total of  $10^3$  to  $3 \times 10^4$  cells are simulated. The beams are then made to cross each other. In the first step, the first layer of the positron beam encounters the first layer of the electron beam. The electric fields are purely transverse to  $O(1/\gamma)$ , and are computed assuming that the charge is located in a sphere located in the center of the cell. This is the “cloud-in-cell” model. Assuming cylindrical coordinates, a cell in beam one gets a total transverse deflection [7]

$$\Delta \mathbf{r}'_{1j} = -\frac{2N_2 r_e}{\gamma} \sum \frac{P_{2i} \mathbf{b}_{ij}}{b_{ij}^2}. \quad (37)$$

The summation runs over the cells in the opposite layer,  $\mathbf{b}_{ij}$  is the impact parameter between cell  $j$  in beam one and cell  $i$  in beam two, and  $P_{2i}$  is the fraction of charge in cell  $i$ . At the end of each layer-layer interaction positions and velocities are updated,

$$\mathbf{r}'_j = \mathbf{r}'_j + \Delta \mathbf{r}'_j, \quad (38)$$

$$\mathbf{r}_j = \mathbf{r}_j + \mathbf{r}'_j \Delta z. \quad (39)$$

$\Delta z$  is the unit step taken along the beam direction. This allows for dynamic beams, with each beam pinching the other as the collision progresses, and the luminosity is computed as an overlap of the dynamic density functions.

The program of reference [10] was found to be unfit for the simulation of flat beams. If the lattice is chosen to have the same number of cells in each dimension, the cells will be as flat as the beam. If the charge is then concentrated in the centers, a large force will be calculated, where in reality the total force is small, due to the cancellations of the large  $x$  components in the integral over the cells. Figure 14 illustrates this.

To reduce this problem the number of cells in  $x$  should be enlarged to make each cell square in the transverse plane. This solution is very CPU time-consuming. A solution was found by replacing each cell with a line of charge, called a “matchstick,” and computing the integral

$$\Delta \mathbf{r}'_{ij} = \frac{-2N_2 r_e P_i}{\gamma} \int dx_i dx_j \frac{\mathbf{b}_{ij}}{b_{ij}^2}. \quad (40)$$

For the purpose of improving the convergence of the program, the matchsticks were kept horizontal throughout the interaction. Assuming matchstick lengths  $L_i$  and  $L_j$ , the solution to the integral above is

$$\Delta \mathbf{r}'_{ij} = \frac{-2N_2 r_e P_i}{\gamma} \left( \sum_1^4 t_n f_n + 2b_y g_n, \sum_1^4 2t_n g_n - b_y f_n \right), \quad (41)$$

where

$$t_1 = b_x + \frac{L_i + L_j}{2} \quad (42)$$

$$t_2 = b_x + \frac{L_i - L_j}{2} \quad (43)$$

$$t_3 = b_x - \frac{L_j + L_i}{2} \quad (44)$$

$$t_4 = b_x + \frac{L_j - L_i}{2} \quad (45)$$

$$f_n = (-1)^{n+1} \log(t_n^2 + b_y^2) \quad (46)$$

$$g_n = (-1)^{n+1} \tan^{-1}(t_n/b_y). \quad (47)$$

Given the deflection vector,  $\mathbf{r}'$ , the total radiated energy with both  $x$ - and  $y$ - polarization is computed using

$$\mathbf{F} = \frac{\gamma m c^2}{2\Delta z} \Delta \mathbf{r}'. \quad (48)$$

The energy vector  $\mathbf{U}$  for each beam is computed by summing

$$U_x = \sum \Delta U_{xj} = \sum \frac{2N}{3mc^2} P_j r_e \gamma^2 F_x^2 \Delta z, \quad (49)$$

$$U_y = \sum \Delta U_{yj} = \sum \frac{2N}{3mc^2} P_j r_e \gamma^2 F_y^2 \Delta z. \quad (50)$$

The program continues to interact the beams, layer by layer, updating trajectories with Equations 38-39, until the beams fully cross each other. An

Quantity	Bin= $0.25\sigma$	Bin= $0.3\sigma$	Fit	Analytic	Dyn.beams
$U_x(10^{12}\text{eV})$	.4002	.3979	.4055	.4051	.4088
$U_y(10^{12}\text{eV})$	.4013	.3997	.4049	.4051	.4163
$L/L_0$	1.00	1.00	1.00	1.00	1.12

Table 2: Comparison between two different binnings, the fitted values, according to Equations 51-52, and the analytic predictions, all for stiff beams. The last column shows the same quantities for dynamic beams.

option was inserted in the program to use or not to use Equations 38-39, that is to make the beams either dynamic or stiff. The reason for the option was to compare against existing analytic predictions for beamstrahlung given in reference [6].

## Appendix C

The simulation program described above is used to make comparisons with the analytic predictions of reference [6] which are valid only for stiff beams. A slow, quadratic convergence was found when diminishing the cell size. When a cell of one beam overlaps with one from the other beam, the program computes a zero field. In reality, the contribution of nearby particles is important, due to the  $1/b$  dependence of the field. Because the emitted power depends on the field squared, the dominant convergence is quadratic.

To adjust for this fact using finite computer resources two different lattice sizes  $a$  and  $b$  were used. The “exact” emitted energy  $U_{ex}$  was extracted using the linear system

$$U_a = U_{ex} - \alpha a^2, \quad (51)$$

$$U_b = U_{ex} - \alpha b^2, \quad (52)$$

and solved for  $U_{ex}$  and  $\alpha$ .

The stiff-beam comparison of  $\mathbf{U}$ , with different cell sizes and against the analytic predictions of reference [6] using the beam parameters of Table 4 are shown in Table 2. There is agreement between analytic and simulation at the 0.2% level. If the beams are dynamic particles will move during the collision by about 1 micron, leaving the beam virtually unchanged in  $x$  but generating a substantial ( $O(10\%)$ ) squeezing in  $y$ . The squeezing will have two effects: it will increase the luminosity and it will generate slightly more power. There will also be a slight asymmetry between  $x$  and  $y$  and some net



polarization. The luminosity increases by 12%. The luminosity calculation was checked, for round beams, against the program of reference [10] and our simulation agrees to within 1%. Figure 15 shows the analytical versus simulation comparison of  $U_y/U_x$  when two flat beams are separated by a vertical offset. We conclude that our simulation method has a precision of order few per thousand for beamstrahlung computations.

## References

- [1] P. Bambade, SLAC-CN-303, 1985; P. Bambade *et al.*, Phys. Rev. Lett. 62: 2949, 1989.
- [2] D. Sagan, J. Sikora and S. Henderson, CBN-97-13.
- [3] G. Bonvicini and J. Welch, CLNS-97-1523, to be published in Nuclear Instruments and Methods.
- [4] J. D. Jackson, "Classical Electrodynamics", Chapter 14.
- [5] D. Cinabro *et al.*, Phys. Rev. E 57, 1193, 1998.
- [6] M. Bassetti *et al.*, IEEE Trans. Nucl. Science 30: 2182, 1983.
- [7] J. D. Jackson, "Classical Electrodynamics", Chapter 11.
- [8] G. Bonvicini *et al.*, Phys. Rev. Lett. 62: 2381, 1989.
- [9] R. Coisson, Phys. Rev. A 20, 524, 1979.
- [10] R. Hollebeek, Nucl. Instr. and Meth. 184, 331, 1981.

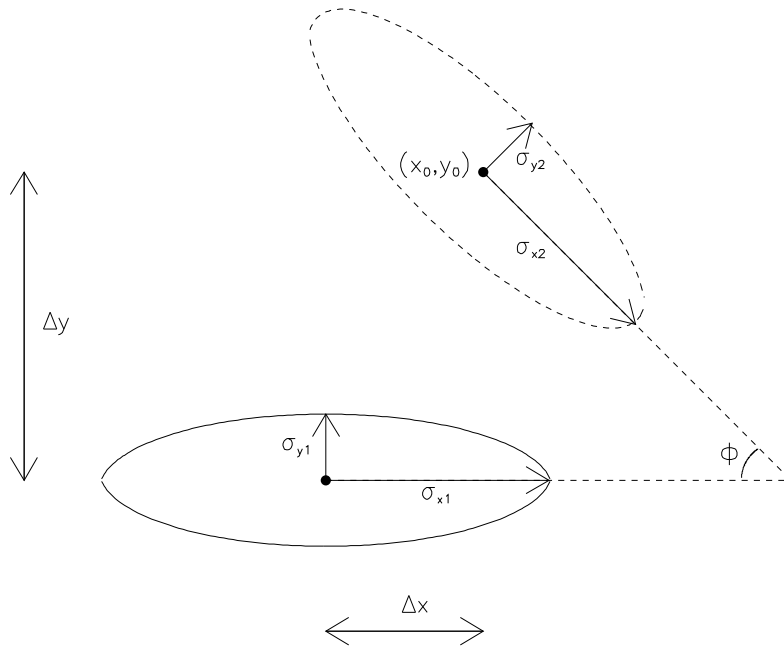


Figure 1: A general beam-beam collision. Seven parameters can be seen, corresponding to two transverse dimensions for each beam, a two dimensional impact parameter vector connecting the two beam centers, and one relative rotation in the transverse plane.

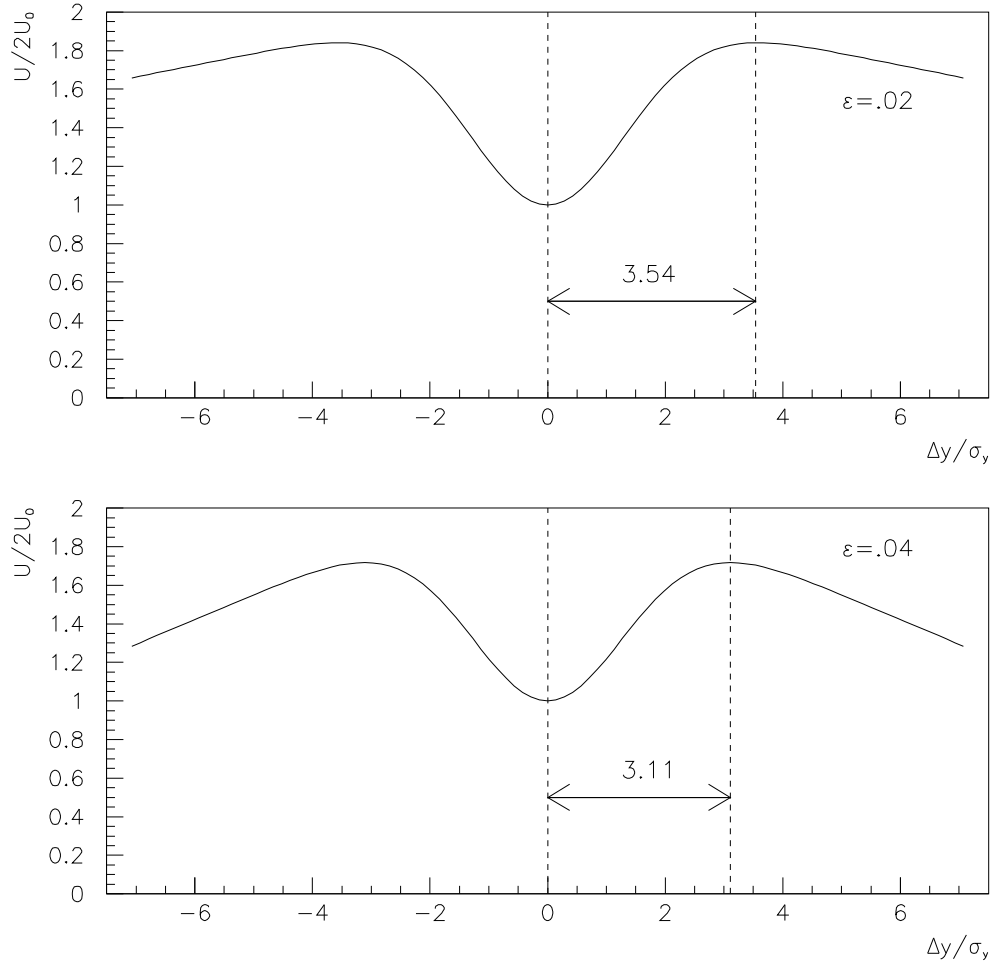


Figure 2: Normalized power emitted in beamstrahlung, as a function of normalized  $y$ -offset. a)  $\epsilon = 0.02$ . b)  $\epsilon = 0.04$ . The distance from minimum to maximum is shown, in units of  $\sigma_y$ .  $U_0$  is defined in Section 4.

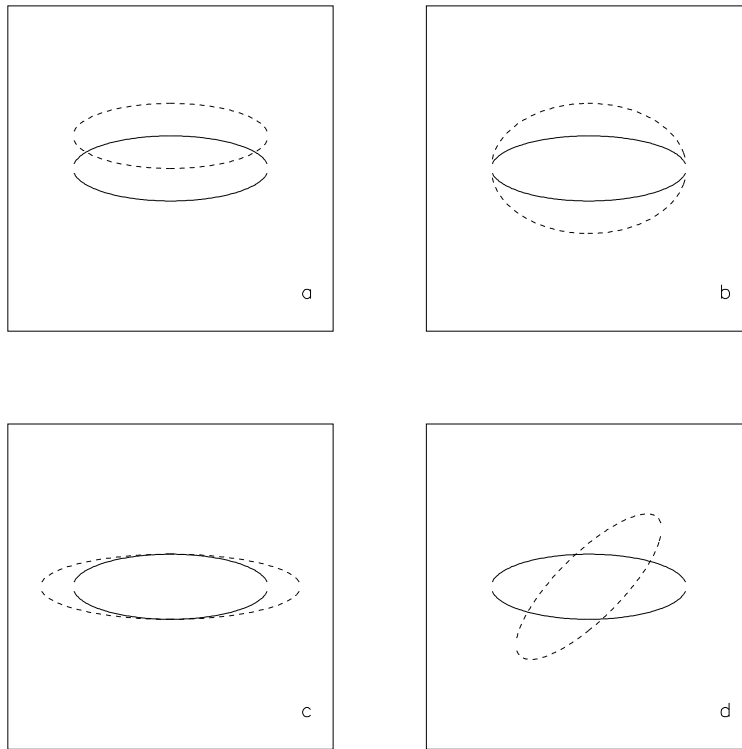


Figure 3: The four beam-beam pathologies that lead to wasted luminosity; a) a  $y$ -offset; b)  $y$ -bloating; c)  $x$ -bloating; and d) a beam-beam rotation. The pathological beam is represented by the dashed ellipse.

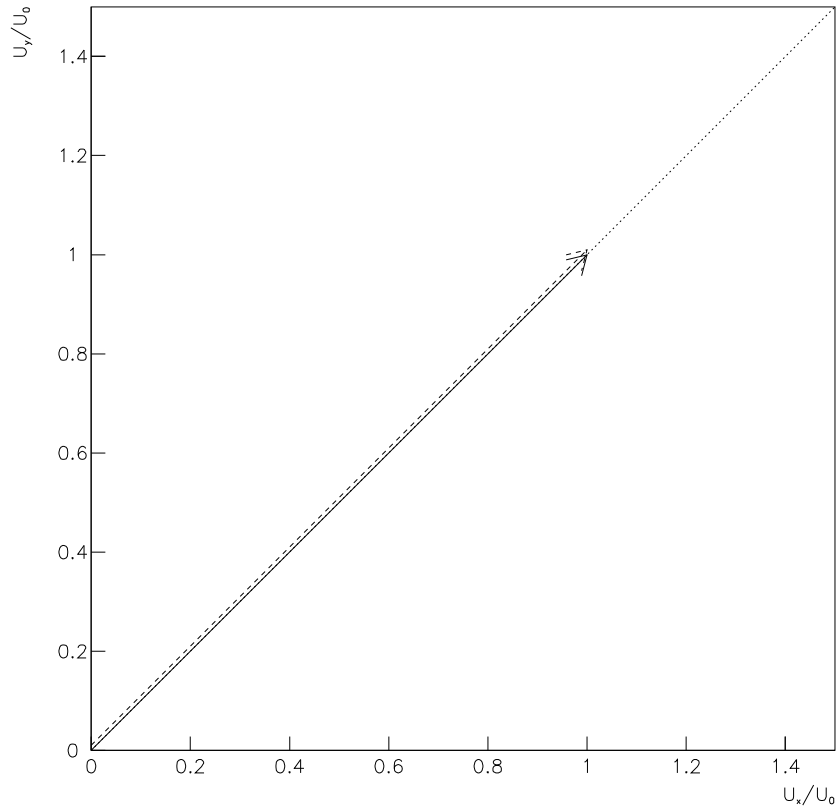


Figure 4: The beamstrahlung diagram corresponding to a perfect beam-beam collision. The two vectors are exactly equal. The dashed arrow is slightly displaced for display purposes.

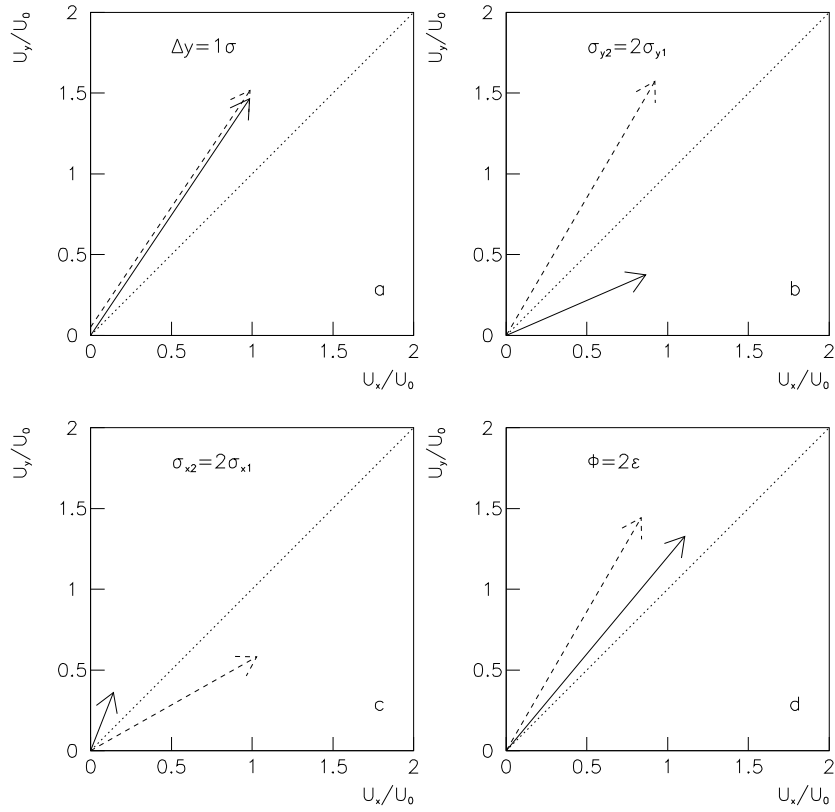


Figure 5: Beamstrahlung diagrams corresponding to the four pathologies of Figure 3. The tips of vectors in part a are displaced for display purposes. Stiff beams are assumed.

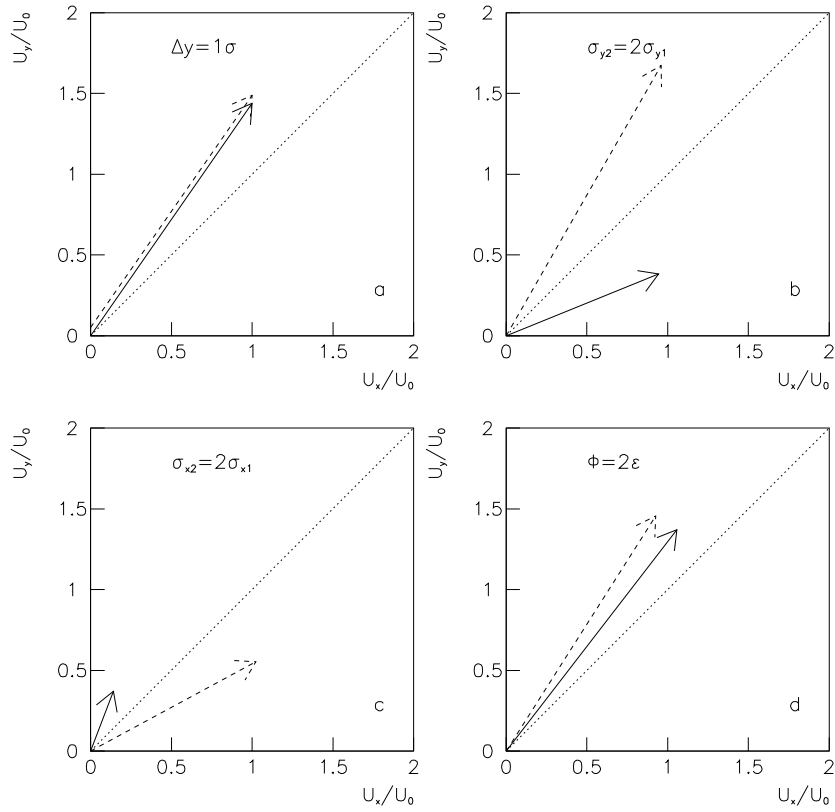


Figure 6: Beamstrahlung diagrams for the same conditions as Figure 5, but assuming dynamic beams.

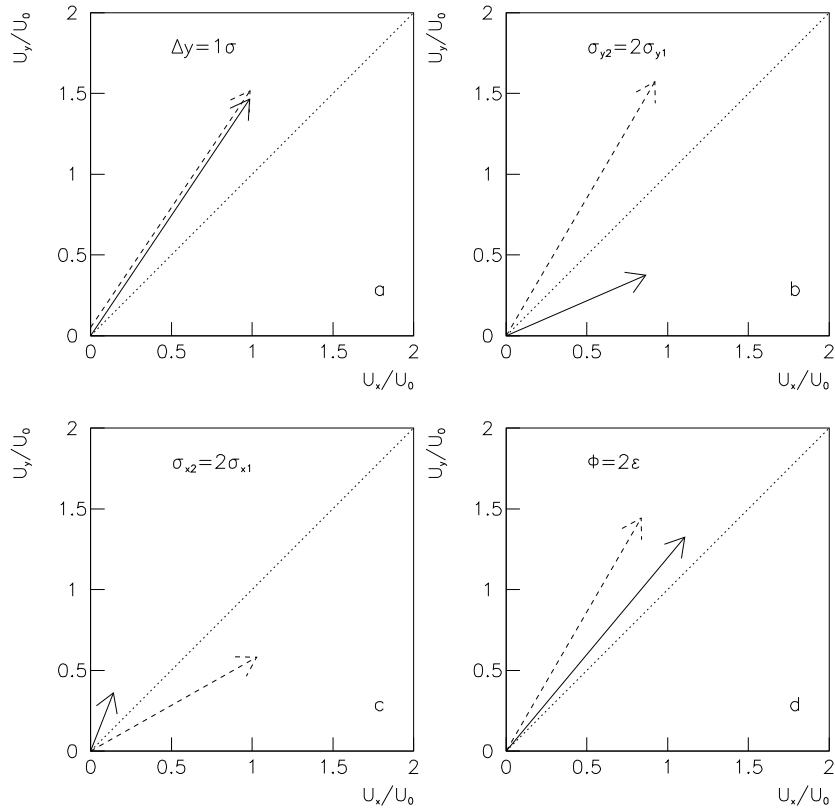


Figure 7: Beamstrahlung diagrams for the same conditions as Figure 5, but assuming an  $x$ -offset of  $0.06\sigma_x$ .



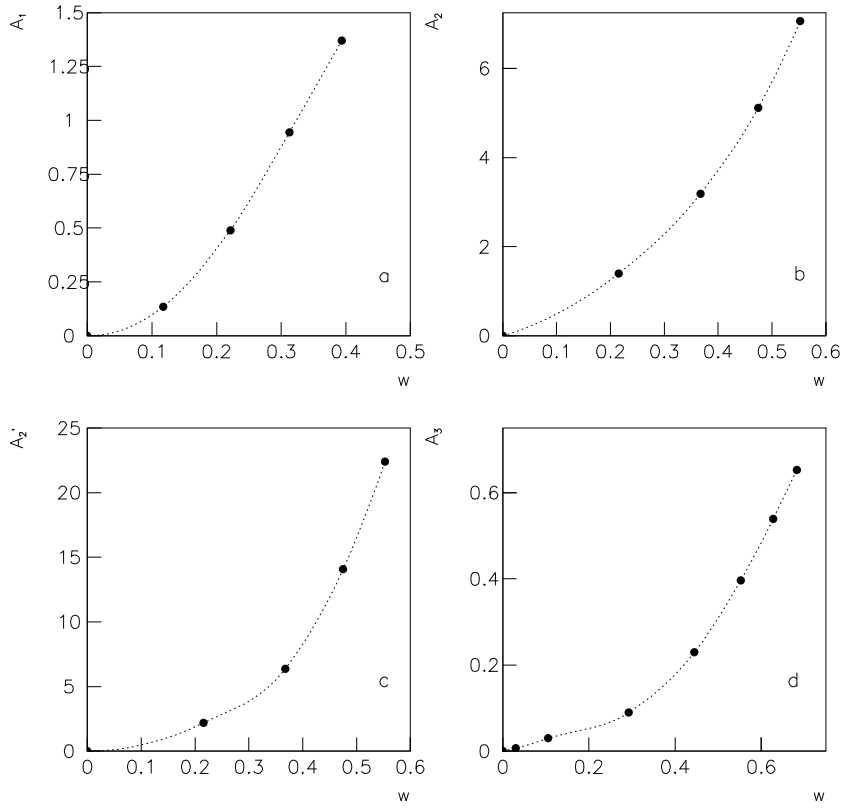


Figure 8: Functional dependence of the beamstrahlung asymmetries defined in the text versus the waste parameter of Equation 3.

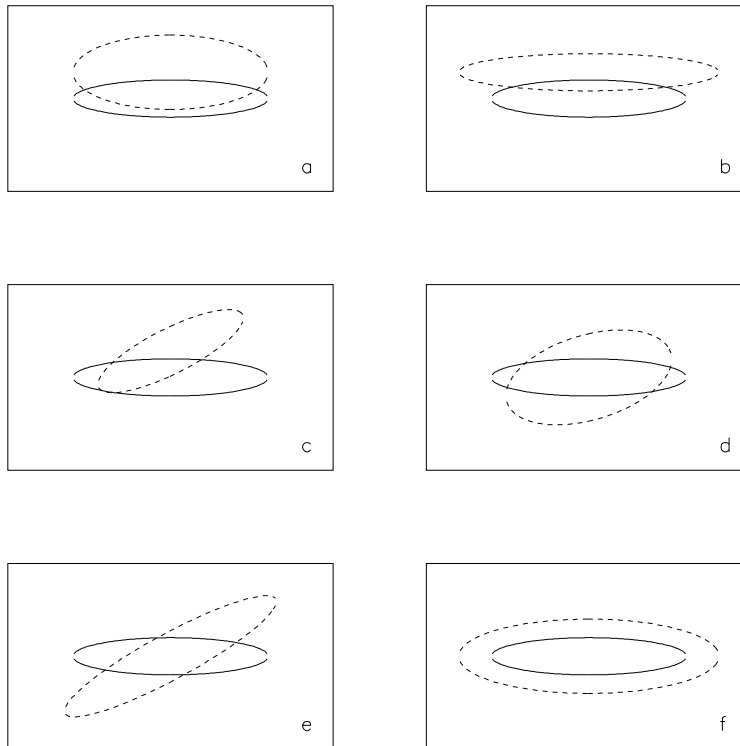


Figure 9: The six possible configurations arising from combinations of any two of the pathologies of Figure 3. a)  $y$ -offset and  $y$ -bloating. b)  $y$ -offset and  $x$ -bloating. c)  $y$ -offset and beam-beam rotation. d)  $y$ -bloating and beam-beam rotation. e)  $x$ -bloating and beam-beam rotation. f)  $y$ -bloating and  $x$ -bloating.

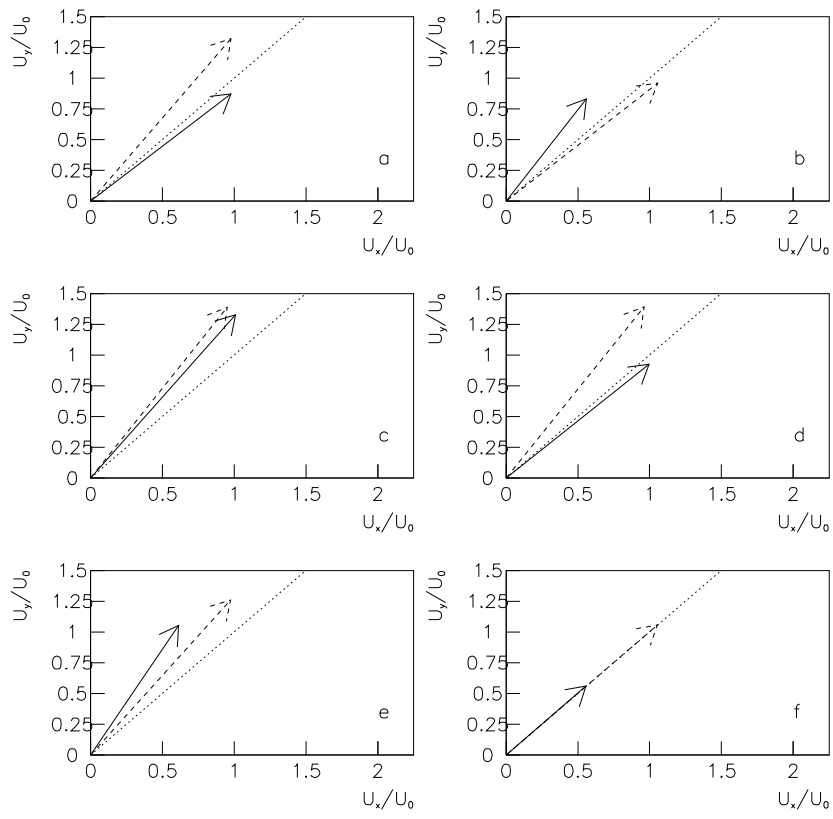


Figure 10: Beamstrahlung diagrams corresponding to Figure 9.

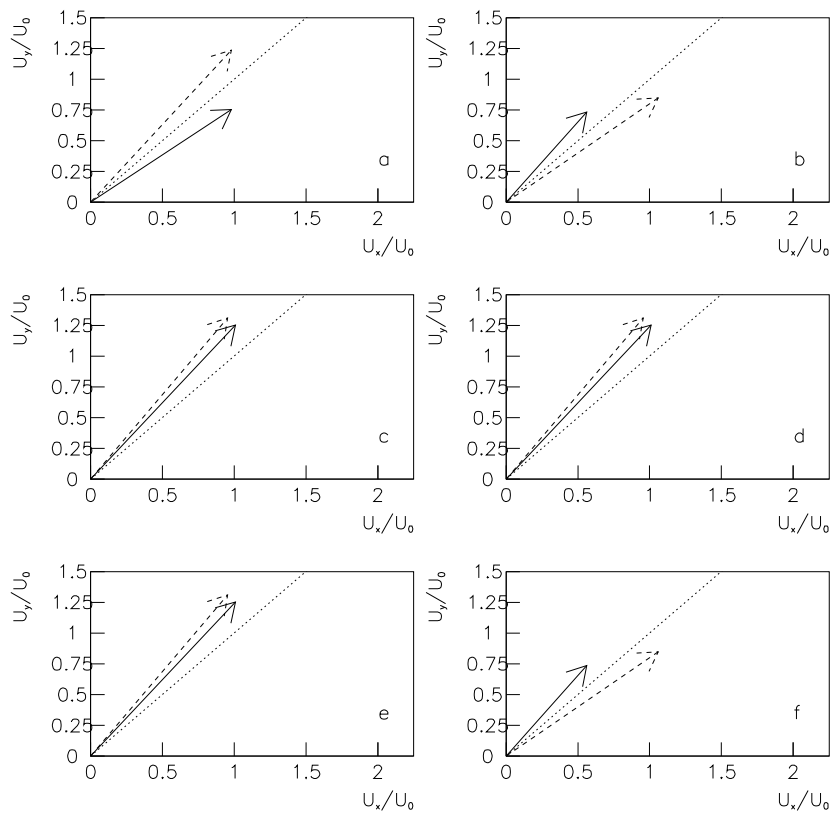


Figure 11: Beamstrahlung diagrams, corresponding to Figures 9 and 10, after correction of the dominant asymmetry. Compare with Figure 3.

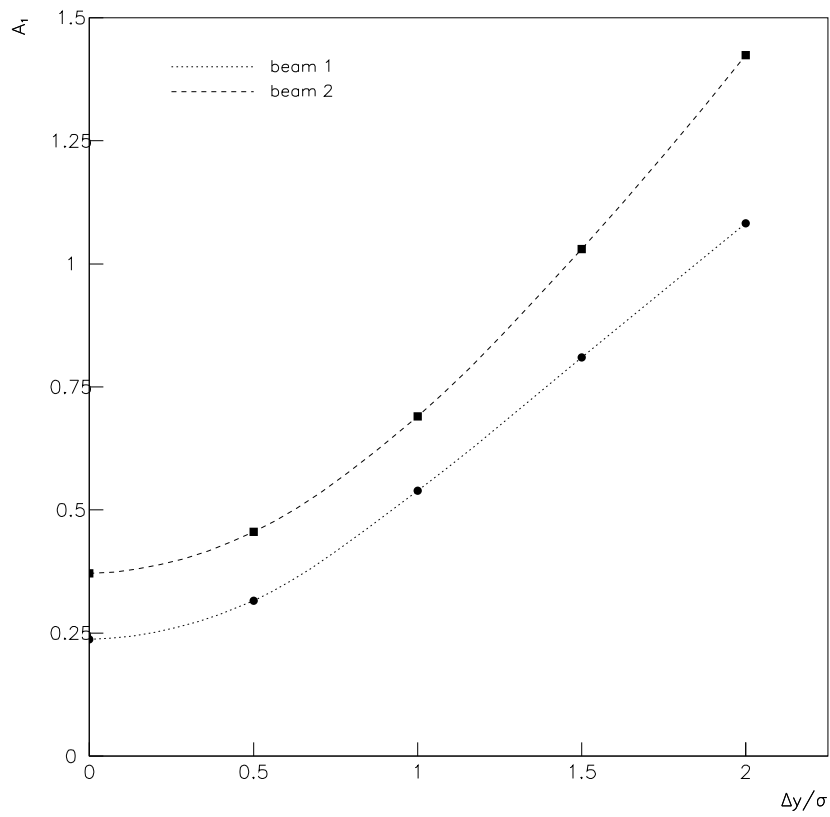


Figure 12: The dependence of the first asymmetry  $A_1$ , as defined in the text, versus the vertical offset for the case of a vertical offset plus a rotation.

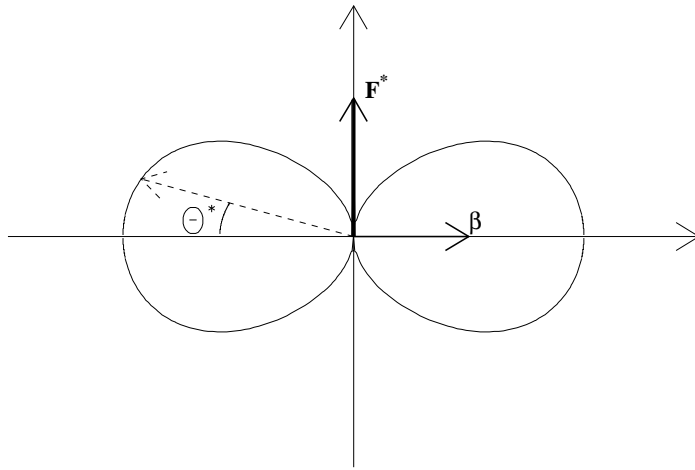


Figure 13: Dipole radiation in a radiating particle's rest frame. Indicated are the direction of the force and the angle corresponding to the observation angle in the laboratory frame.

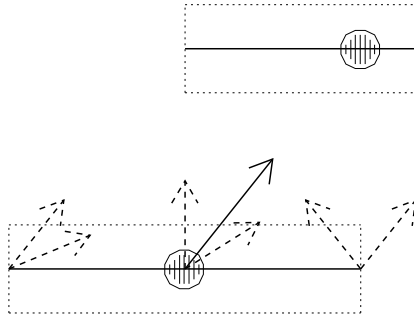


Figure 14: Cell-cell interaction in the simulation program. The cell has an aspect ratio similar to the beam aspect ratio. In the “cloud-in-cell” model, all the charge is concentrated in a point in the center of the cell. In the “matchstick-in-cell” model, the charge is spread over a line along the cell.

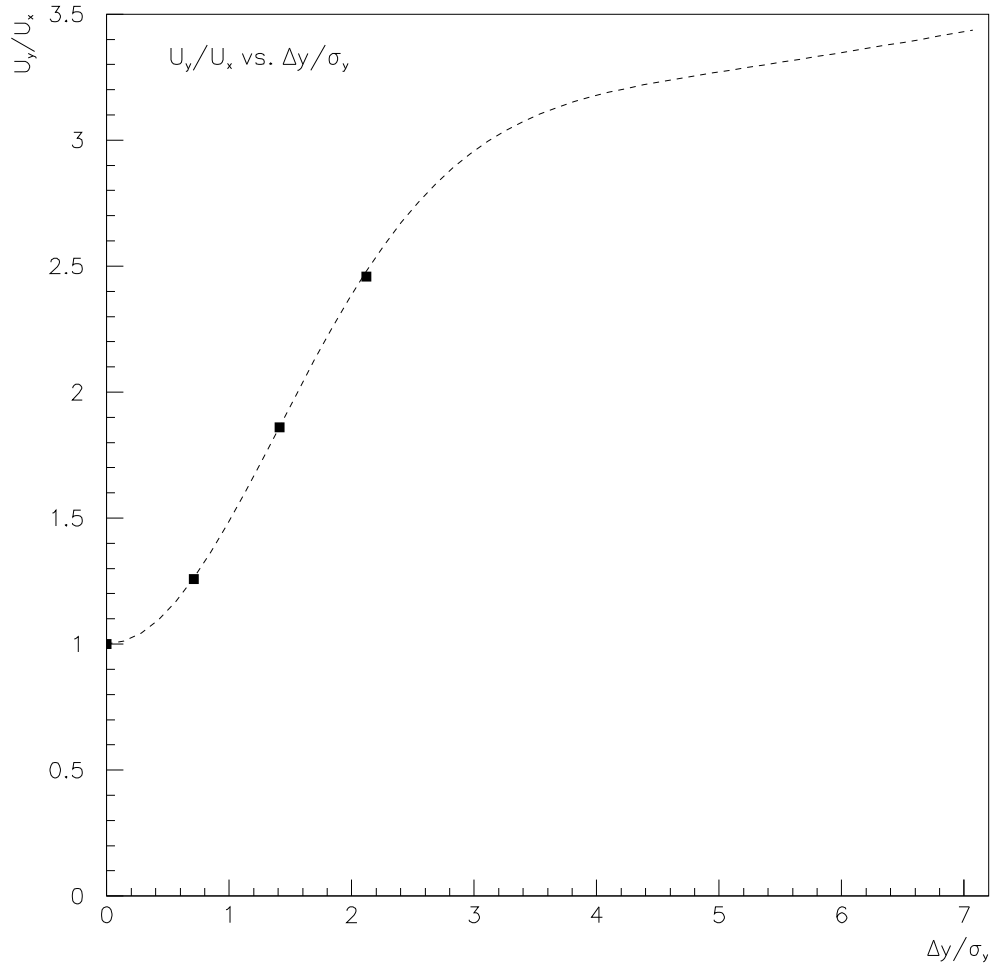


Figure 15: Radiation polarization versus beam-beam offset. The solid line is the analytic prediction from reference [6], and the dots are from the simulation described in the text.